Response of the atmospheric boundary layer to a mesoscale oceanic eddy in the northeast Atlantic

Denis Bourras, Gilles Reverdin, Guy Caniaux, Hervé Giordani

Response of the atmospheric boundary layer to a mesoscale oceanic eddy in the northeast Atlantic

Denis Bourras[1] and Gilles Reverdin

Laboratoire d'Océanographie Dynamique et de Climatologie, Paris, France

Hervé Giordani and Guy Caniaux

Centre National de Recherches Météorologiques, Toulouse, France

[1] Fields of air-sea turbulent fluxes and bulk variables were derived from satellite sensor data from February to April 2001, over a region of the northeast Atlantic where a field experiment, Programme Océan Multidisciplinaire Meso Echelle (POMME), was conducted. The satellite products are in good agreement with in situ data in terms of heat fluxes, sea surface temperature, and wind speed. The central part of the experimental domain presented a cyclonic eddy in the ocean, which corresponded to a cold sea surface temperature (SST) anomaly. Winds were weaker within the eddy than outside of it, with lower latent and sensible heat loss. In order to analyze the relationship between the SST and wind anomalies, three numerical experiments were conducted with a regional atmospheric model. Three 3-month runs of the model were performed, using a realistic SST field, a smoothed SST field in which the cold SST was not present (reference run), and an SST field where the cold anomaly was increased by two degrees, successively. The fields simulated with the realistic SST were consistent with satellite sensor derived observations. In particular, the weak wind area over the cold SST anomaly was successfully rendered, whereas it was not present in the forcing fields. Taken individually, the three runs did not reveal the presence of secondary circulations. However, anomalous secondary circulations were clearly identified with respect to the reference run. The origin of the latter circulations was investigated with the Giordani and Planton generalization of the Sawyer-Eliassen equations. According to our results, differential heating induced by the cold SST anomaly mostly altered the vertical wind through the effect of friction and only marginally through pressure gradient forces. In the upper part of the boundary layer, the wind speed increased (decreased) over (downstream) the cold SST. We found that stability was the main factor that induced the simulated patterns of the friction term in the diagnostic equations. Therefore our results show that mesoscale wind patterns were significantly affected by SST gradients through the effect of stability, in a region of low oceanic eddy activity.   *INDEX TERMS:* 3307 Meteorology and Atmospheric Dynamics: Boundary layer processes; 3329 Meteorology and Atmospheric Dynamics: Mesoscale meteorology; 3339 Meteorology and Atmospheric Dynamics: Ocean/atmosphere interactions (0312, 4504); 3360 Meteorology and Atmospheric Dynamics: Remote sensing

1. Introduction

[2] The study of air-sea interactions is important for our understanding of climate variability, because the exchanges of heat and momentum that take place between the sea and the atmosphere control, in part, the circulations of these two media at a wide range of timescales and space scales.

[3] The response of the marine atmospheric boundary layer (MABL) to a sea surface temperature (SST) gradient is an example of air-sea interaction that was extensively studied over the last two decades. This phenomenon is analogous to the land or sea breeze effect, in which the thermal contrast between land and sea creates a horizontal pressure gradient. In turn, the pressure gradient alters the surface level wind on either side of the coast line and can generate cross frontal secondary circulations, or SCs [*Wexler*, 1946]. Over water, the mechanism through which

---

[1]Now at Institut Pierre-Simon Laplace, Centre d'étude des Environnements Terrestre et Planétaires, CNRS, UMR 8639, Vélizy-Villacoublay, France.

the MABL reponds to a SST gradient is still an open question, because pressure gradient forces compete with other mechanisms such as the horizontal gradient of stability of the MABL, which affects turbulent mixing and subsequently friction against the sea surface, and wind. The response of the MABL to a SST gradient encompasses several other aspects that are not yet fully understood, such as the characteristics of the SCs and the role of timescales and space scales. The present paper is an attempt to document the above mentioned aspects on the basis of a well identified situation, in which an oceanic eddy influenced the MABL for three months in the northeast Atlantic. In this section, we first present a review of the relevant literature. Next, the present situation is described.

1.1. Background

[4] *Sweet et al.* [1981] reported the results of a 2-day aircraft observational campaign in the vicinity of the Gulf Stream. The first day, the aircraft flew from the cold waters north of the north wall to the warm SSTs of the Gulf Stream. As the aircraft was crossing the SST front, these authors noticed a significant increase in near surface wind at 61 m above sea level (8–12 kt), and a ~70% rise in boundary layer height (BLH). They also observed an evolution in static stability, from stable to unstable, and in cloudiness, from clear sky to broken stratocumulus clouds. On the basis of their observations, they hypothesized that the stabilizing effect of the cold water [...inhibited the development of stronger winds through vertical transfer of momentum].

[5] Over much weaker SST contrasts (~1°C), *Businger and Shaw* [1984] showed that the horizontal gradients of turbulent fluxes of momentum and heat followed the SST gradients on 1 September 1978, during the Joint Air-Sea Interaction Experiment (JASIN) [*Pollard*, 1978]. This can be interpreted as a first refinement of *Sweet et al.* [1981] results; namely, the SST-induced differential heating of the MABL generates a horizontal stability gradient through heat fluxes. In turn, stability affects the drag coefficient and subsequently, the wind stress.

1.2. SCs

[6] *Businger and Shaw* [1984] further speculated on how the airflow would behave over a "warm" oceanic eddy. The SST induced surface wind stress gradient would result in surface wind convergence on the upwind edge of the eddy and divergence on the downwind edge. This convergence/divergence effect can be associated with solenoidal SCs.

[7] An accurate diagnostic of SCs is difficult to obtain because on one hand, the available instruments are inadequate, which implies that only indirect observations or model simulations of the SCs are achievable, and on the other hand the structure of the SCs can be rather complex.

[8] Indications of the presence of SCs were found over weak and strong SST gradients during three experiments: the Frontal Air-Sea Interaction Experiment near the Bermudas (FASINEX [*Stage and Weller*, 1985; *Khalsa and Greenhut*, 1989; *Friehe et al.*, 1991]), the Genesis Altantic Lows Experiment (GALE [*Warner et al.*, 1990]), in the vicinity of the Gulf Stream, and the Structure des Echanges Mer-Atmosphère Propriétés des Hétérogénéités Océaniques: Recherche Expérimentale experiment (SEMAPHORE [*Eymard et al.*, 1996; *Kwon et al.*, 1998; *Giordani et al.*,

1998]), near the Azores islands. *Giordani and Planton* [2000] (GP2000 hereafter) simulated the response of the MABL for one day of SEMAPHORE. Their simulation is perhaps one of the most convincing to date, as it clearly shows the presence of a surface induced cellular ageostrophic circulation.

[9] The relationship between the vertical extent of the SCs and the surface forcing conditions is an issue that has never been fully elucidated. For SEMAPHORE, GP2000 found ~200 m or one fourth of the MABL height, which indicated the existence of an Internal Boundary Layer (IBL). An IBL was also observed by *Rogers* [1989] during FASINEX, also over a weak SST gradient but for a cold SST anomaly. In contrast, the extent to which the MABL is affected by SST gradients was found to be large in the eastern equatorial Pacific, where the SST gradients are themselves large [*Xie et al.*, 1998; *Hashizume et al.*, 2002]. The latter authors analyzed radiosonde data along the path of a Japanese research vessel that cruised across three tropical instability waves (TIW) at 2°N, in September 1999. They provided evidence that the full extent of the MABL was affected by the variations of the SST, as they observed correlated variations between BLH and SST. Altogether, these results suggest that the larger the SST gradient is, the higher the SC vertically extends. This remains to be further investigated.

1.3. Timescales and Space Scales

[10] With the availability of the first global in situ data sets such as the Comprehensive Ocean-Atmosphere Data Set (COADS [*Woodruff et al.*, 1987]), it was shown that the MABL responded to the SST gradients over a wide range of timescales and space scales, namely, from 20 days to the interannual scale in timescales and from the mesoscale to a basin wide scale, according to *Wallace et al.* [1989] and *Hayes et al.* [1989]. More recent studies that used satellite-derived winds and SSTs also support this hypothesis. For example, *Chelton et al.* [2001] have shown similarities between SST and wind variations in the eastern tropical Pacific at scales on the order of 20 days. *White and Annis* [2003], who focused on four other regions of intense eddy activity, namely, the Kuroshio, the Gulf Stream, the Antarctic circumpolar current, and the Brazil current, found cause to effect relationships between SST and wind variations at space scales and timescales of 400–1200 km and 6 months, respectively.

[11] While these results clearly show the long-term effect of strong SST gradients on the MABL, what remains unclear is to which extent weak SST gradients associated with mesoscale eddies present in the majority of the world's ocean have an impact on the MABL. This kind of eddies has received little attention in the previous studies that used spatial data sets. Furthermore, eddies were always studied statistically, i.e., large populations of eddies and not individual eddies, except for the TIW eddies observed in *Chelton et al.* [2001].

1.4. Originating Mechanisms

[12] Two main factors may explain how a SST front induces an ageostrophic circulation, namely, pressure-gradient forces and horizontal variations of stability that affect mixing and thus friction at the sea surface. A large

majority of papers have supported the latter hypothesis so far, most of them dealing with strong SST gradients [e.g., *Xie et al.*, 1998]. Over weak SST gradients, the question is still open. For instance, GP2000 used sophisticated diagnostic tools, a generalization of the diagnostic equations of *Sawyer* [1956] and *Eliassen* [1962] (S−E equations hereafter) and the ω-equation of *Hoskins et al.* [1978], for analyzing the response of the MABL to the Azores front. They found that the different terms in the equations contributed equally to the generation of ageostrophic circulations; that is, friction did not dominate during SEMAPHORE, according to these authors. They pointed out that additional terms should be taken into account in order to explain the generation of ageostrophic circulations, both of dynamical and thermal origins. *Cronin et al.* [2003] recently raised this issue while analyzing the response of the MABL to TIWs with satellite observations and moored buoy data. They studied the vertically integrated meridional momentum balance near the equator, and found that advection by the mean wind was not negligible.

1.5. Present Case Study

[13] In the present manuscript, we report three months of observations of a mesoscale cyclonic oceanic circulation associated with a cold SST anomaly, and its influence on the MABL. The cyclonic oceanic feature was found while analyzing data of the intensive observation period (IOP) of the Programme Océan Multidisciplinaire Meso Echelle (POMME, Multidisciplinary Mesoscale Ocean Program) experiment, which was conducted in 2000 and 2001 in the northeast Atlantic, that is, in a region where eddy activity is weaker than in the western part of the Atlantic [*Ducet et al.*, 2000]. A circular mesoscale structure in air-sea fluxes and wind speed was clearly identified over the cold SST anomaly, using satellite and drifting buoy data. These observations are statistically reliable since they correspond to averages from February to April, i.e., to many kinds of environmental (and especially wind) conditions. Numerical experiments were then conducted in order to (1) analyze the sensitivity of wind speed and boundary layer characteristics to the SST gradient, (2) investigate whether SCs were generated by the surface temperature gradient, (3) assess the height reached by the vertical circulations, and (4) find the mechanisms through which the ocean affected the organization of the MABL.

[14] In the next section, the data used are presented. Next, the POMME region is described, and the evidence of a circular structure persistent for three months both in the ocean and in the atmosphere is shown (section 3). In section 4, the response of the boundary layer characteristics to the cold SST anomaly is analyzed. In section 5, we identify the leading process responsible for the MABL response, and conclusions are given in section 6.

2. Data

[15] The POMME experiment was conducted in a region delimited by 15°20′W/21°20′W and 38N/45N. The data used throughout this study correspond to the POMME IOP, from 1 February 2001 to 30 April 2001. Fields of SST, wind, and surface fluxes were derived from four kinds of data, namely, satellite products, operational analyses

from the European Centre for Medium-Range Weather Forecasts (ECMWF) model, drifting buoy measurements, and observations from a research vessel. They are described hereafter.

2.1. SST Analysis

[16] The SST fields used are daily analyses in which in situ SSTs from over a hundred drifters and floats, one mooring, and a ship were merged with Advanced Very High Resolution Radiometer (AVHRR) derived SSTs, as fully described by G. Caniaux et al. (A 1-year sea surface heat budget in the northeastern Atlantic Basin during the POMME experiment, submitted to *Journal of Geophysical Research*, 2004) (hereinafter referred to as Caniaux et al., submitted manuscript, 2004). The spatial resolution of the SST analyses is 5 km.

2.2. Winds

[17] Daily wind fields were derived from both National Aeronautics and Space Administration (NASA) QuikSCAT project scatterometer and the Defense Meteorological Satellite Program Special Sensor/Microwave Imagers (DMSP-SSM/I), F13, F14, and F15. The daily QuikSCAT wind vector fields were provided by Institut Franais de Recherche pour l'Exploitation de la Mer (Ifremer), while SSM/I scalar winds were derived from SSM/I brightness temperatures using the algorithm of *Goodberlet et al.* [1990]. As the SSM/I wind retrievals were strongly biased when large amounts of cloud liquid water (CLW) were present in the atmosphere, a CLW retrieval algorithm was used to reject cloudy situations for which CLW was greater than $0.3 \, \text{kg m}^{-2}$ [*Gérard and Eymard*, 1998]. The instantaneous individual wind retrievals that were used to produce daily fields were compared to wind measurements performed onboard l'Atalante, a ship from Ifremer. Data within ±0.1° and ±10 min were selected for the comparison. Since the SSM/I and QuikSCAT winds are given at heights of 19.5 m and 10 m, respectively, ship winds that were measured at 17.5 m were converted to these heights for the comparison, with a bulk algorithm. The results of the comparisons are reported in Table 1. The rms accuracies of the retrieved winds are $0.92 \, \text{m s}^{-1}$ for QuikSCAT and $1.74 \, \text{m s}^{-1}$ for the SSM/I. Note that the rather large error in SSM/I derived winds is within the nominal error of the *Goodberlet et al.* [1990] algorithm ($\pm 2 \, \text{m s}^{-1}$).

[18] Twenty-one drifting buoys were launched from L'Atalante during the POMME IOP. These buoys, called Marisonde in the following, are developed and operated by Météo-France (French meteorological office). The sensors mounted on the Marisonde buoys measure sea level pressure (SLP), SST, and wind speed at a height of 2 m. For the present study, the data collected were used for deriving a wind field, intended to validate the mesoscale features of the satellite-derived wind fields. Note that a correction was applied to the Marisonde winds, because the measurements are relative to the ocean current. The wind correction consists in a daily estimate of the surface current, which was calculated with the daily evolution of the locations of the buoys.

[19] The Marisonde data collected each day from 10 February (the first day for which data from at least five Marisondes were available simultaneously) to 30 April

Table 1. Comparison of Instantaneous Satellite-Derived Variables and ECMWF Operational Analyses With Ship Data Averaged Over 20 min[a]

Variable	Source	Unit	Correlation	rms	Bias	Linear Fit
u_A	SSM/I	m s^{-1}	0.85	1.74	0.00	$0.86x + 1.15$
	QuikSCAT	...	0.97	0.92	0.41	$1.01x + 0.34$
	ECMWF	...	0.92	1.30	0.03	$0.93x + 0.67$
SST	analyses	°C	0.97	0.21	−0.06	$0.93x + 0.97$
θ_A	ECMWF	...	0.86	0.65	0.74	$0.94x + 1.52$
q_A	...	g kg^{-1}	0.92	0.54	0.16	$0.90x + 0.92$
L_E	...	W m^{-2}	0.92	19.7	−13.1	$0.85x − 2.78$
	satellite	...	0.81	29.3	15.4	$0.77x + 30.9$
H_S	ECMWF	...	0.81	8.20	−9.64	$0.77x − 7.48$
	satellite	...	0.82	7.52	−0.42	$0.88x + 0.64$
Longwave	ECMWF	...	0.72	18.43	−10.75	$0.70x − 2.04$
(1 day)	satellite	...	0.92	9.92	−0.13	$1.40x + 13.5$
Shortwave	ECMWF	...	0.77	45.44	−15.18	$0.88x + 58.7$
(1 day)	satellite	...	0.98	15.36	−2.91	$1.12x − 15.5$

[a]For the comparisons of the longwave and shortwave fluxes, data were averaged over 1-day periods.

2001 were interpolated in the following fashion. Each day, the mean position of the buoys in latitude and longitude was used to generate a triangulated area on which the data were linearly interpolated. Next, the interpolated winds were projected on regular grids at the resolution of 50 km. Finally, the gridded wind fields were averaged over the IOP.

2.3. Surface Fluxes

[20] The net heat flux is the sum of four fluxes, namely, the sensible (H_S) and latent (L_E) turbulent heat fluxes, plus the longwave (infrared) and shortwave (solar) radiative fluxes. Longwave and shortwave fluxes were derived from Meteosat radiances at Météo-France following the processing method of *Brisson et al.* [1994]. L_E was derived from a combination of SSM/I brightness temperatures and SSTs from the analyses described above. The retrieval algorithm used is based on artificial neural networks [*Bourras et al.*, 2002a]. The *Gérard and Eymard* [1998] algorithm was also used here for avoiding cloudy situations. The sensible heat flux algorithm is an air temperature horizontal advection model that uses wind vectors from the QuikSCAT scatterometer and SST analyses as inputs [*Bourras et al.*, 2002b]. It also uses air temperatures at 17 m (θ_A) from ECMWF analyses as boundary conditions. The lapse rate of radiative cooling is a constant in the advection model. It was empirically adjusted, in order to remove an average bias in air temperature with respect to ship data. Finally, the different flux fields were combined and interpolated to obtain daily surface net heat flux fields at the resolution of 30 km.

[21] Validation of the different flux fields (turbulent, radiative, and net flux) was performed with respect to ship observations, and is reported by Caniaux et al. (submitted manuscript, 2004). ECMWF analyses extracted four times daily at the resolution of 0.5° were also compared to ship data. The results of the comparisons are summed up in Table 1. For the latent and sensible heat fluxes, the rms deviation between satellite and ship fluxes are 30 W m^{-2} and 7.5 W m^{-2}, respectively. This is ∼10 W m^{-2} larger than the rms between ECMWF and ship fluxes, for the latent heat flux. Note however that the advantage of the satellite data over operational analyses is their "constant" mesoscale resolution, while the effective resolution of meteorological models depends on the number of assimilated data [*Bourras et al.*, 2003]. The difference in bias of

the different fluxes with respect to ship data are large (e.g., 29 W m^{-2} for L_E). The consequences of this, in the context of ocean forcing, are discussed in detail by Caniaux et al. (submitted manuscript, 2004). It also means that the absolute values of the satellite flux fields used in this study are not as accurate as those of ship data. However, this does not question the present work, as one is mainly interested in identifying mesoscale air sea processes, i.e., in the spatial variability of the satellite-derived variables.

3. A Mesoscale Anomaly in Wind and SST

[22] This section starts with a brief description of the environmental conditions that prevailed from 1 February to 30 April 2001 over the POMME area. Next, emphasis is laid on mesoscale features present in the fields of oceanic and atmospheric variables, and on their evolution during the three months.

3.1. Description of the IOP Winds, Fluxes, and SSTs

[23] During the IOP, the most common synoptic situation was characterized by an anticyclonic circulation South of the region and a cyclonic circulation to the N−NE (Figure 1e). Mean winds and SSTs over the three months were near climatological values, that is, 8−9 m s^{-1} and ∼14.4°C, respectively, as reported in Table 2. SSTs were warmer to the S−SW, as shown in Figure 1a. The net heat flux (positive downward) was negative until the first days of March and positive thereafter, indicative of spring ocean warming. During the three months, SSTs (θ_A) increased by 0.4°C (0.3°C), while wind intensity decreased by ∼1.1 m s^{-1}. In the meantime, the net heat flux increased by ∼130 W m^{-2}, which resulted from the increase in solar flux. The daily variations of SLP, winds, and latent heat flux indicate that at least five depressions crossed the POMME region. The first one, on 5−6 February was more severe (993 hPa), with peaks in latent heat flux (∼200 W m^{-2}) and wind (∼15 m s^{-1}), as well as a temporary decrease in SST, by 0.1°C. Altogether, the POMME IOP is representative of typical late winter or spring midlatitude conditions.

3.2. Mesoscale Features

[24] Fields of analyzed SSTs and satellite-derived winds and net heat fluxes clearly reveal that the POMME region is
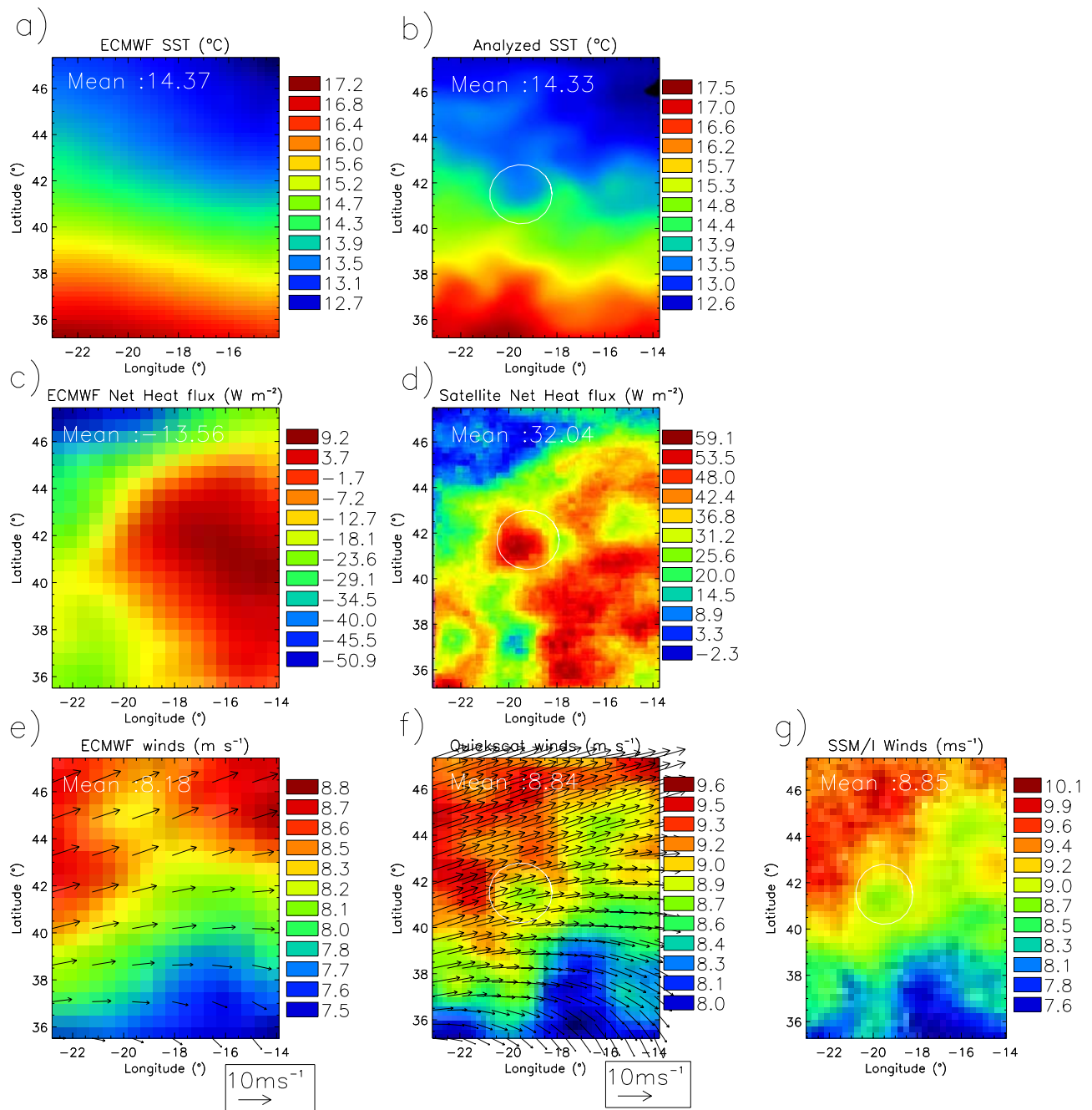
Figure 1. Spatial distribution of (a, c, e) ECMWF and (b, d, f, g) satellite environmental variables over the POMME region from 1 February to 30 April 2001. Circles in white locate an anomaly present in the satellite-derived fields only. Note that the color scales in Figures 1a and 1b, in Figures 1c and 1d, and in Figures 1e, 1f, and 1g are different, in order to better compare the spatial variations of the SST, net flux, and wind.

dominated by mesoscale features in the 3-month average, as shown in Figures 1b, 1d, 1f, and 1g. The average wavelength of the structures in Figures 1d and 1f is ~250 km. These mesoscale structures, present in fields of both oceanic and atmospheric variables, do not appear in the ECMWF fields, even though satellite-derived wind vectors were assimilated in the ECMWF model (Figures 1a, 1c, and 1e). Note, however, the good overall agreement between ECMWF and satellite-derived fields of net flux, SST, and

wind, for the large scale spatial variations. Differences in biases between satellite and model products are large, especially for the net flux, as already discussed in section 2.

[25] A prominent mesoscale feature in Figure 1b is a circular SST anomaly of ~1°C, centered on 41.5N/19.5W, with a 90 km radius. This SST feature is rather weak compared to the anomalies found in strong currents like the Gulf Stream, which may reach 10 times what is found here. Here it corresponds to a cyclonic circulation, as revealed by

Table 2. Mean Values and 3-Month Evolution (Maximum Minus Minimum Value of the Linear Fit to the Data) of Atmospheric and Oceanic Variables Over the POMME Region

Variable	Source	Unit	Mean Value	Evolution
u_A	ECMWF	m s^{-1}	8.18	−1.15
	SSM/I	...	8.86	−1.16
SST	analyses	°C	14.31	+0.40
SLP	ECMWF	hPa	1016	+5
q_A	...	g kg^{-1}	7.7	+0.1
θ_A	...	...	14.1	+0.8
L_E	...	W m^{-2}	59.7	−3.8
	satellite	...	87.2	−7.8
H_S	ECMWF	...	1.9	−3.4
	satellite	...	7.6	+2.8
Net flux	ECMWF	...	13	+134
	satellite	...	51	+129
Shortwave flux	ECMWF	...	135	
	satellite	...	153	+131
Longwave flux	ECMWF	...	−43	
	satellite	...	−26	+1.8

circulation analyses produced by *Assenbaum and Reverdin* [2004], in which satellite-derived sea level anomalies as well as in situ measured currents and oceanic density profiles were assimilated (not shown). This cyclonic circulation appears to have a core that has remained in the vicinity of 41.5N/19.5W during the three months. For this

reason and for simplicity, the cyclonic circulation is called "eddy" in the following. This eddy is surrounded by two warm anticyclonic circulation zones located at 18W/42N and 21W/42N, respectively. In these regions, found just east and west of the cold eddy in Figure 1b, the SST was more variable than at the location of the cold eddy, during the 3-month period.

[26] The SST anomaly associated with the cold eddy is clearly visible in Figure 1d as a positive net heat flux anomaly, which means that the ocean gained heat at the location of the eddy. The flux anomaly appears in the turbulent flux fields, but not in the downward radiative flux fields (Figure 2), which suggests that the flux feature is a surface induced effect. More surprising is the presence of a mesoscale wind anomaly that perfectly fits the location and dimensions of the cold eddy, in two independent satellite sensor derived wind fields (Figures 1f and 1g). Note that the color scales used in Figures 1f and 1g are different, in order to better compare the spatial variations of the satellite-derived wind fields. The maximum intensity of the wind gradient across the anomaly is ∼0.7−0.9 m s^{-1} per 100 km. It could be a coincidence that two independent sensors detected the circular anomaly, since its magnitude is smaller than the accuracy of both satellite products (1−2 m s^{-1}). However, the feature is also present in the Marisonde buoy wind analyses (section 2.2), as shown in Figure 3. It is
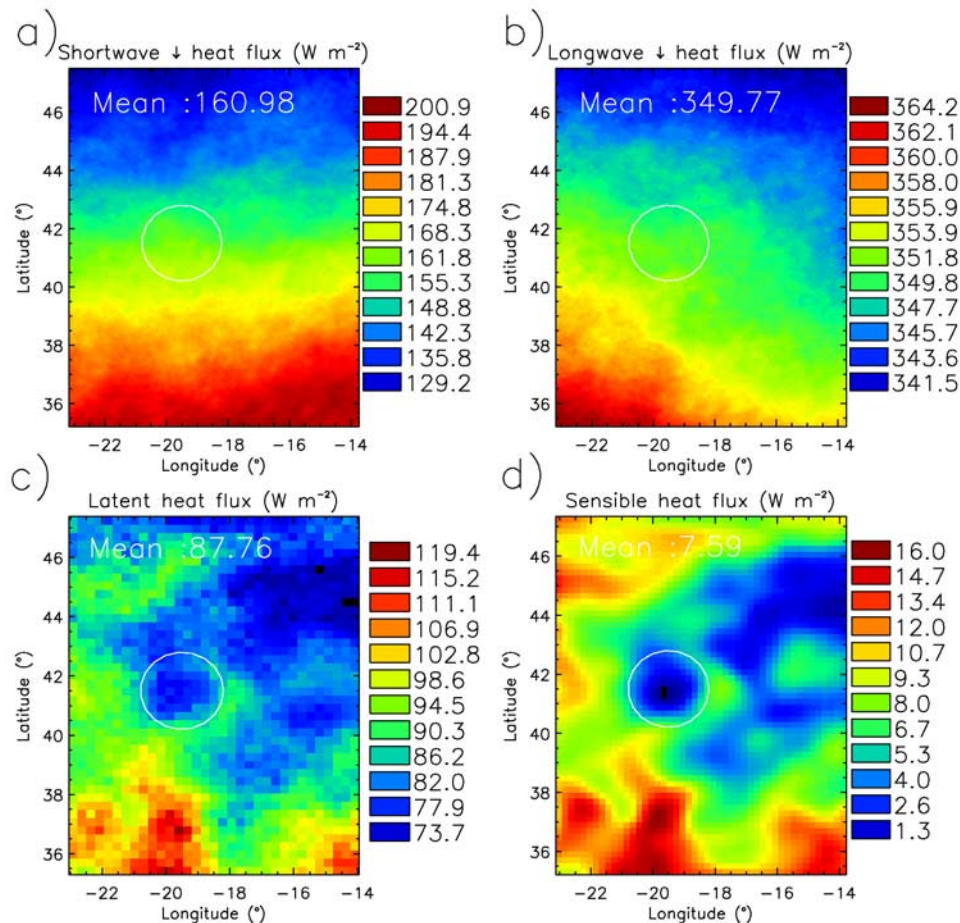

Figure 2. Surface fields of (a, b) satellite-derived downward radiation fluxes, (c) latent heat flux, and (d) sensible heat flux from 1 February to 30 April 2001.
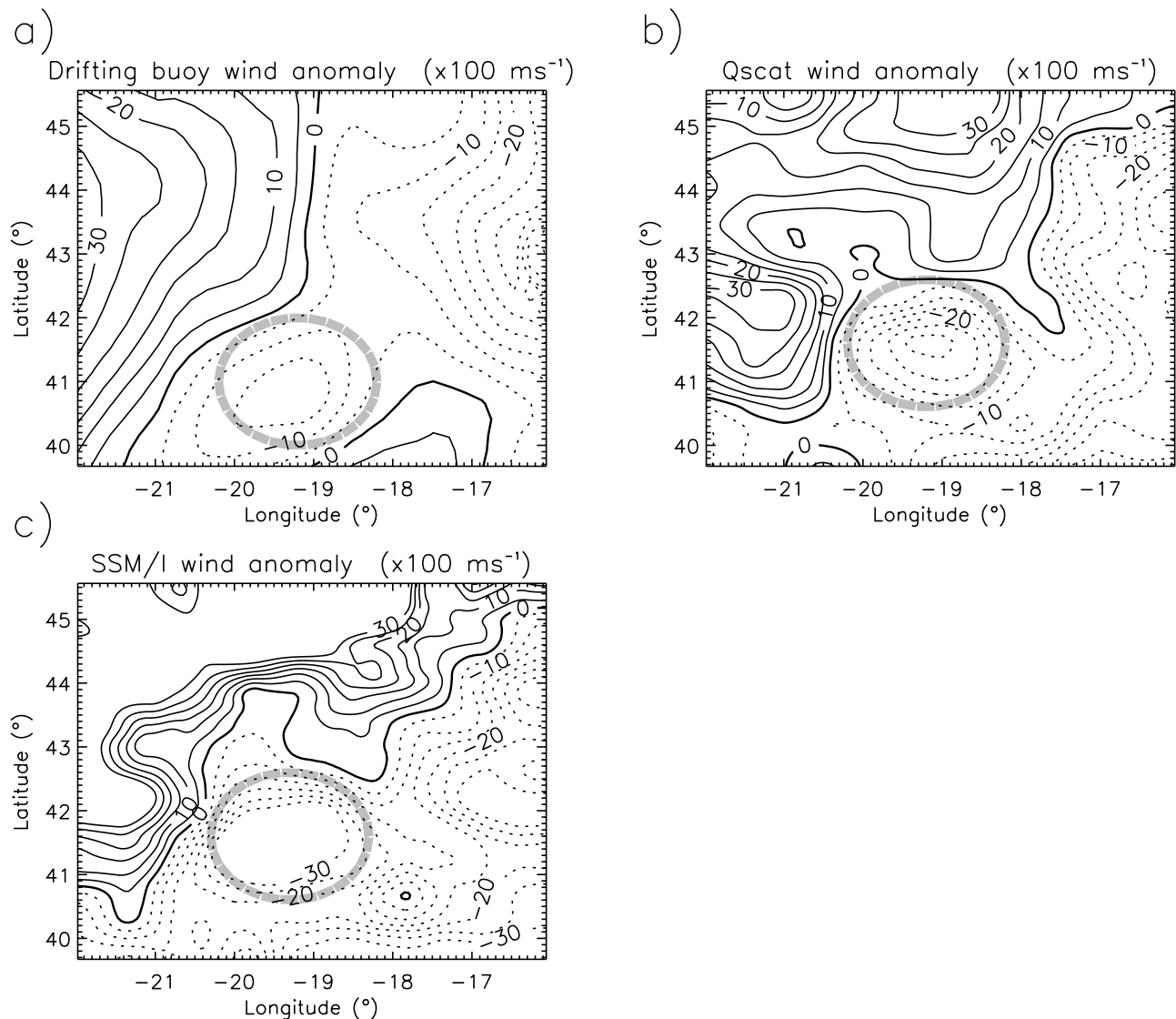
a)

b)

c)

Figure 3. Spatial distribution of scalar wind speed anomalies derived from (a) Marisonde drifting buoys and (b, c) two satellite sensors. Positive (negative) contours are plotted in full (dotted) line. The fields correspond to averages from 11 February to 30 April 2001. The circles in grey locate a negative wind speed anomaly associated with a cyclonic circulation in the ocean. Contour intervals are 0.05 m s^{-1}.

slightly shifted southward (40.8N) with respect to its location in the satellite fields, which possibly results from sparsity of interpolated Marisonde data. The maxima of the wind speed gradients taken between 22W and 19.5W are 0.28, 0.85, and 0.64 m s^{-1} per 100 km, according to the Marisonde, SSM/I, and QuickSCAT data, respectively. It shows that the wind gradient is weaker according to the Marisonde data than in the satellite observations.

[27] On the basis of these first results, one may suspect that the SST anomaly affects the surface wind pattern through its effect on surface fluxes. Indeed, the wind and SST anomalies are in phase; that is, the wind slows down over the cold SST and accelerates after, as in *Hashizume et al.* [2002], for instance.

3.3. Evolution of Wind and SST Anomalies

[28] To get further insight about the possible relationship between the SST anomaly and the surface wind, it is interesting to analyze its day to day variations. This is needed to explain the statistical relevance of the 3-month average, which can be either the cumulative effect of many individual daily occurrences, or the result of a strong event that would affect statistics at the scale of three months. It can also happen only for specific wind situations.

[29] The time evolution of wind and SST anomalies is presented in Figure 4 along a cross section from 22W/40.5N to 17W/42.5N. This cross section was chosen because it crosses the center of the SST anomaly and is aligned with the direction of the 3-month mean wind. Wind and SST anomalies were computed as follows. For each day, the linear fit (mean plus trend) along the cross section was removed from the data. Next, a low pass Gaussian filter, with a cutoff frequency of ~100 km was applied (to wind data only). There was no filtering in time.

[30] The SST anomaly was remarkably steady in location and intensity during February and March, as shown in
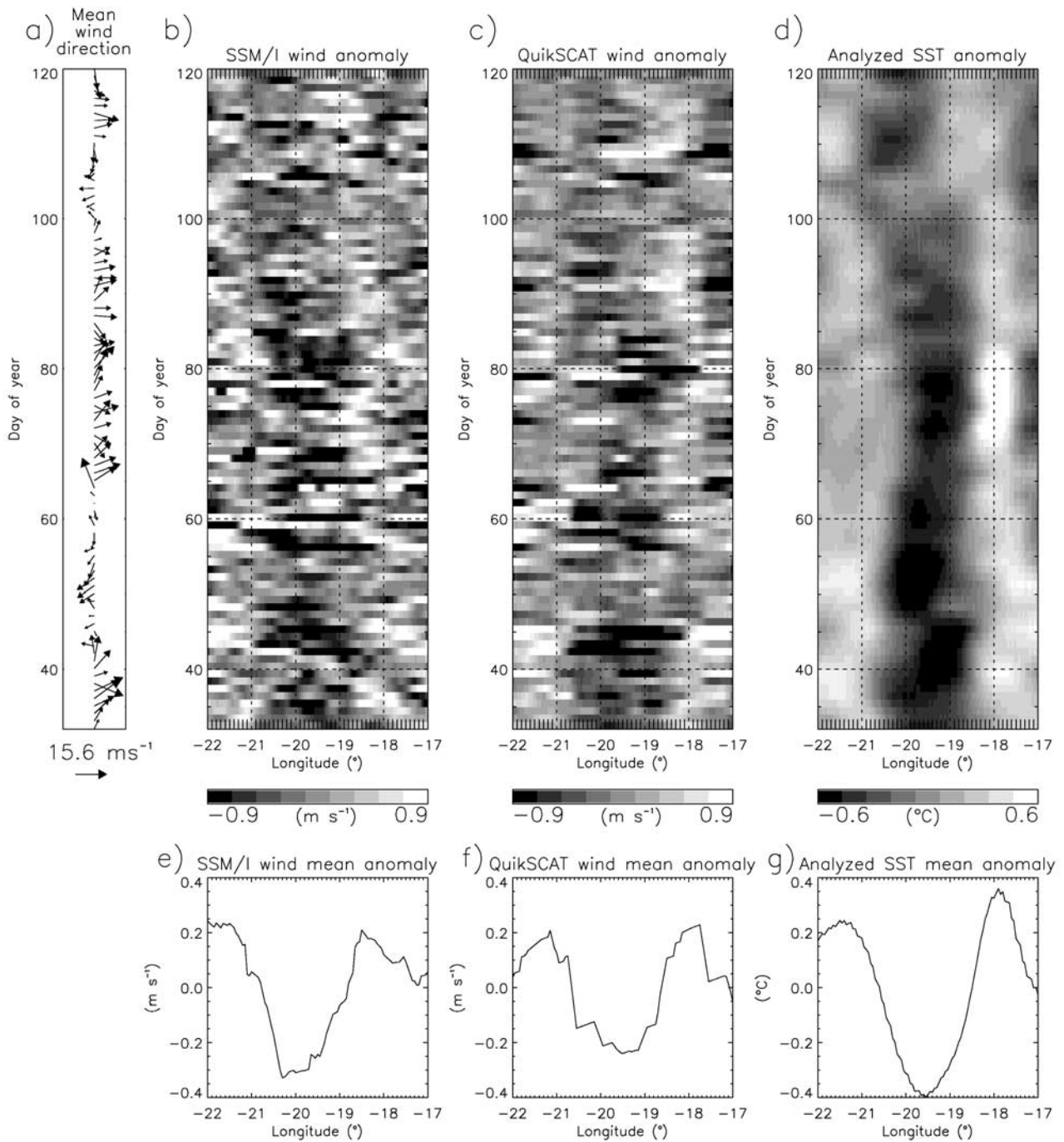
Figure 4. Evolution of (a, b, c) satellite-derived wind direction and wind speed anomalies, and (d) analyzed SST anomalies along a cross section from 22W/40.5N to 17W/42.5N. (e, f, g) Associated horizontal profiles averaged from 1 February to 30 April 2001.

Figure 4d. It started to move westward by ~50 km, after 10 April (day 100 in Figures 4a–4d), and presented a temporary loss of intensity on 14–16 February. Note also that the SST contrast was the strongest from 6 March to 26 March (days 65 to 85), because of an increase in warm SST, east of the cold eddy.

[31] Wind anomalies both from SSM/I and QuikSCAT observations are noisy, in spite of the spatial filtering (Figures 4b and 4c), which is not surprising given the small

magnitude of the mean wind anomaly (previous section). However, a darker band at the location of the SST feature is clearly distinguishable in both Figures 4b and 4c. It follows the westward shift of the SST feature after day 100, which confirms the existence of a relationship between wind and SST. Moreover, although the wind anomaly is not continuous, it is visible every 1 to 10 days. This shows that the wind-SST relationship found for the 3-month average is statistically significant, since it was generated by at least

Table 3. Mean Values and Standard Deviation of Atmospheric and Oceanic Variables Simulated With MM5

Variable	Unit	Mean Value	Standard Deviation
u_A	m s^{-1}	7.8	0.4
q_A	g kg^{-1}	8.1	0.7
θ_A	°C	13.9−14.2	1.4
L_E	W m^{-2}	87−91	12−13
H_S	...	0−1	3
Net heat flux	...	7−13	19−20
Shortwave heat flux		145−147	20
Longwave heat flux	...	−46	6

10 events during three months. The intensity of the wind anomaly is not correlated with the wind direction at the instantaneous scale, which is likely related to the fact that the SST anomaly is small (Figures 4a–4d). In order to investigate whether the wind-SST relationship depended on wind direction for the 3-month average, the wind and SST anomalies were computed separately when wind was blowing eastward and westward. The result (not shown) indicates that there is no strong modification or displacement of the wind anomaly, as a function of wind direction. One may also conclude that advection is not a dominant effect in the wind-SST relationship.

[32] Mean amplitudes of wind and SST anomalies are 0.5−0.6 m s^{-1} and 0.75°C, respectively, according to Figures 4e–4g. The QuikSCAT wind and SST anomalies are in phase, for the 3-month average. They present a minimum around 19.5W, the center of the cold eddy. On the other hand, mean anomalies from QuikSCAT and the SSM/I are not exactly in phase (shift of ∼50 km, i.e., one and a half pixels), which reveals either errors in the satellite algorithms or non perfect data processing (Figures 4e and 4f).

4. Sensitivity of MABL to SST Gradients

[33] A mesoscale meteorological model (MM5) [*Dudhia*, 1993] was used to investigate the relationship between the cold eddy and the overlying wind anomaly observed in section 3. The POMME IOP was simulated with MM5, using various SST fields in which the cold anomaly was present or not, as lower boundary conditions.

[34] Hereafter, the main characteristics of the MM5 simulations are presented. Next, the simulations are validated. Finally, the response of the MABL to the cold eddy is analyzed, at surface level and at ∼1000 m, the MABL height.

4.1. Simulation of the IOP

[35] The MM5 simulations were performed on a domain from 26°W/34°N to 11°W/49°N, which is larger than the POMME area in order to minimize the effect of lateral boundary conditions. The resolution of the model was set to 20.1 km in latitude/longitude, with 23 levels along the vertical in addition to six levels in the boundary layer. The MABL model used is the medium range forecast model (MRF [*Hong and Pan*, 1996]), which was used in MM5 for many years. It is based on a Charnock formulation of the roughness length, for momentum and temperature exchanges [*Betts et al.*, 1996]. For humidity, the calculation

of the roughness length is based on a viscous sublayer model [*Carlson and Boland*, 1978].

[36] Three runs were performed, based on three different types of SST fields. Daily ECMWF SSTs with no mesoscale features (the average of which is shown in Figure 1a) were used for the first run, which is the reference run, referred to as smooth SST run (SSR) in the following. The second run used the daily analyzed SST fields (Figure 1b), and was named realistic SST run (RSR). For the third run, we slightly modified the SSTs of the RSR: the temperature was intentionally decreased by 2°C at the center of the cold eddy. The latter run was called SST Minus Two Run (SM2R). The SM2R was intended to identify particular effects of the SST gradients on the MABL that could appear less clearly in the RSR, because of the smaller magnitude of its SST gradients.

[37] For each run, the model was initialized every day at 0000 UTC, and run for 24 hours, with outputs every 3 hours. ECMWF operational analyses of wind, temperature, humidity, and atmospheric liquid water were used as initial atmospheric boundary conditions. There was no assimilation of any kind during the simulation. This was intended to let the model generate fields as close as possible to the physics of MM5. Let us recall that the wind anomalies shown in section 3.2 were not present in the forcing wind fields (Figure 1e).

4.2. Validation

[38] The validation consists in verifying that the RSR (SSR) MM5 forecasts comply with the satellite-derived (ECMWF) atmospheric variables presented in section 3.2. First, the mean values are compared. Next, the comparison is carried out in terms of spatial variations.

[39] The mean values and standard deviations of the simulated fields averaged over three months are reported in Table 3. The three runs (SSR, RSR, and SM2R) gave very close results. The most affected variable was air temperature, which varied from 13.9°C (SSR) to 14.2°C (RSR and SM2R).

[40] For most of the atmospheric variables, the mean deviations between MM5 and ECMWF are small (Tables 2 and 3). For instance, these deviations are 0.3 m s^{-1} and 0.3 g kg^{-1} for u_A and the specific humidity at 17.5 m (q_A), respectively. The average net heat fluxes from MM5 and the ECMWF model closely correspond to each other. However, this masks differences in individual flux components. Indeed, L_E is ∼29 W m^{-2} larger in MM5 than in the ECMWF analyses and the shortwave flux is ∼11 W m^{-2} larger in MM5 than in the ECMWF model.

[41] The patterns of SSR wind and net flux compare generally well to those of the ECMWF fields, as shown in Figures 1e and 1c, and Figures 5a and 5d (note that the color scales are different in Figures 1 and 5, in order to highlight the spatial variations of winds and net heat fluxes). This suggests that the physics of MM5 and the ECMWF model are consistent. Nevertheless, small differences are noticeable. For instance, the net flux in the western part of the region is smaller in the SSR than in the ECMWF analyses, and a negative wind anomaly present at 20W/45N in the ECMWF field is almost not rendered by MM5.

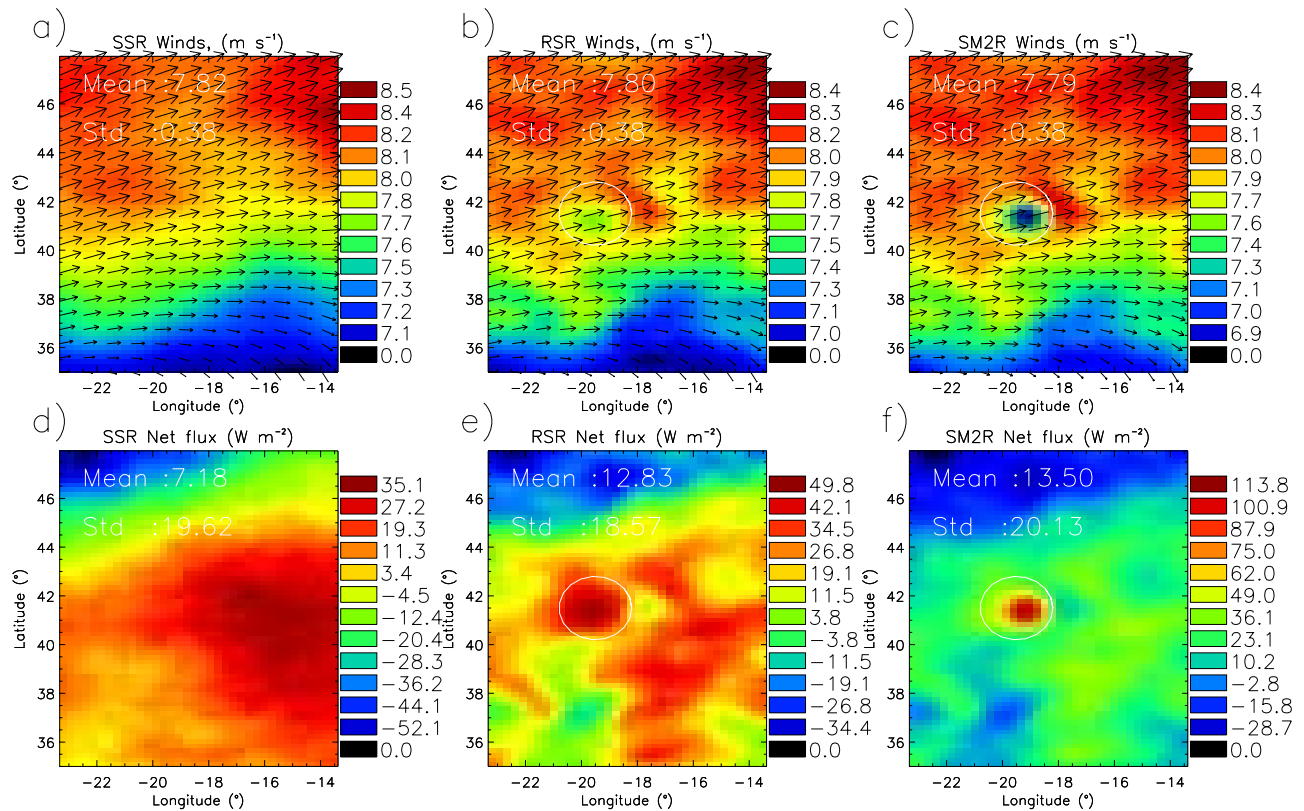[42] Wind and net flux fields from satellite data and the RSR are in very good agreement (Figures 1f and 5b). This

Figure 5. Spatial distribution of surface winds and net heat flux according to the three MM5 simulations. Circles in white locate the cold SST anomaly.

also holds for other parameters such as humidity, air temperature, latent, sensible, and shortwave fluxes. The main differences occur between satellite-derived and simulated cloud cover, integrated humidity, and longwave fluxes (not shown), which possibly indicates some deficiencies in the cloud scheme used. However, the orders of magnitude of the longwave fluxes are correctly simulated by MM5, compared to satellite estimates (Tables 2 and 3).

[43] The SM2R and RSR wind and net heat flux fields exhibit similar patterns for most of the region (compare Figures 5b and 5c, and Figures 5e and 5f). However, wind and flux anomalies are larger in the SM2R than in the RSR at the location of the SST anomaly, as expected.

4.3. Response of the MABL at Sea Level

[44] The wind anomaly present in the satellite-derived fields was successfully simulated with MM5, when MM5 was initialized with a realistic SST field, as reported in the previous section. In contrast, no anomaly was present in the MM5 wind fields at the location of the cold eddy, when the latter eddy was not present in the forcing SST fields. From these two results, one can firmly state that the effect of the cold eddy at 19.5W/41.5N is to slow down surface wind.

[45] According to the RSR simulations, the decrease in wind is ~0.6 m s^{-1} per 100 km, which is smaller by 0.1–0.3 m s^{-1} than the value deduced from satellite observations (section 3.2). The decrease in wind becomes 1.2 m s^{-1} per 100 km if the SST gradient is increased up to 2°C per 100 km (SM2R). If one assumes the existence of a linear relationship between SST and wind gradients, one may extrapolate these values to the following relationship: the

across front wind gradient (in m s^{-1} per 100 km) is 0.6 times the SST gradient (in °C per 100 km), for SST gradients smaller than 2°C.

[46] The signature of the cold eddy is visible on the SM2R and RSR downward radiative fluxes, at surface level (not shown). The longwave flux is decreased over the cold SST while the shortwave flux increases. Additionally, the integrated cloud liquid water decreases over the cold SST. Unfortunately, the satellite-derived fields of radiative fluxes and integrated water do not confirm these results. This possibly means that the flux gradients are too small to be detected by the spaceborne sensors. Indeed, the longwave and shortwave flux gradients are only ~3 W m^{-2} per 100 km in the RSR.

[47] A decomposition of the wind into geostrophic and ageostrophic components is presented in Figure 6. Note that the zone focused on in Figure 6 (and in the following) is restricted to a part of the POMME region that includes the cold eddy and the warm eddy to its east. Figures 6a and 6d reveal a zone of horizontal divergence located over the maximum surface thermal gradient that corresponds to the transition from the cold eddy to the warm eddy. The geostrophic component of the SM2R-SSR wind clearly reveals an anticyclonic circulation, which means that atmospheric pressure is increased over the cold SST (Figure 6c). The anticyclonic circulation is also visible in the RSR-SSR (Figure 6f), though it is attenuated and merged with the synoptic flow. Finally, the ageostrophic component of the wind is clearly correlated to the wind for both the RSR-SSR and SM2R-SSR, which means that ageostrophic circulations dominate the
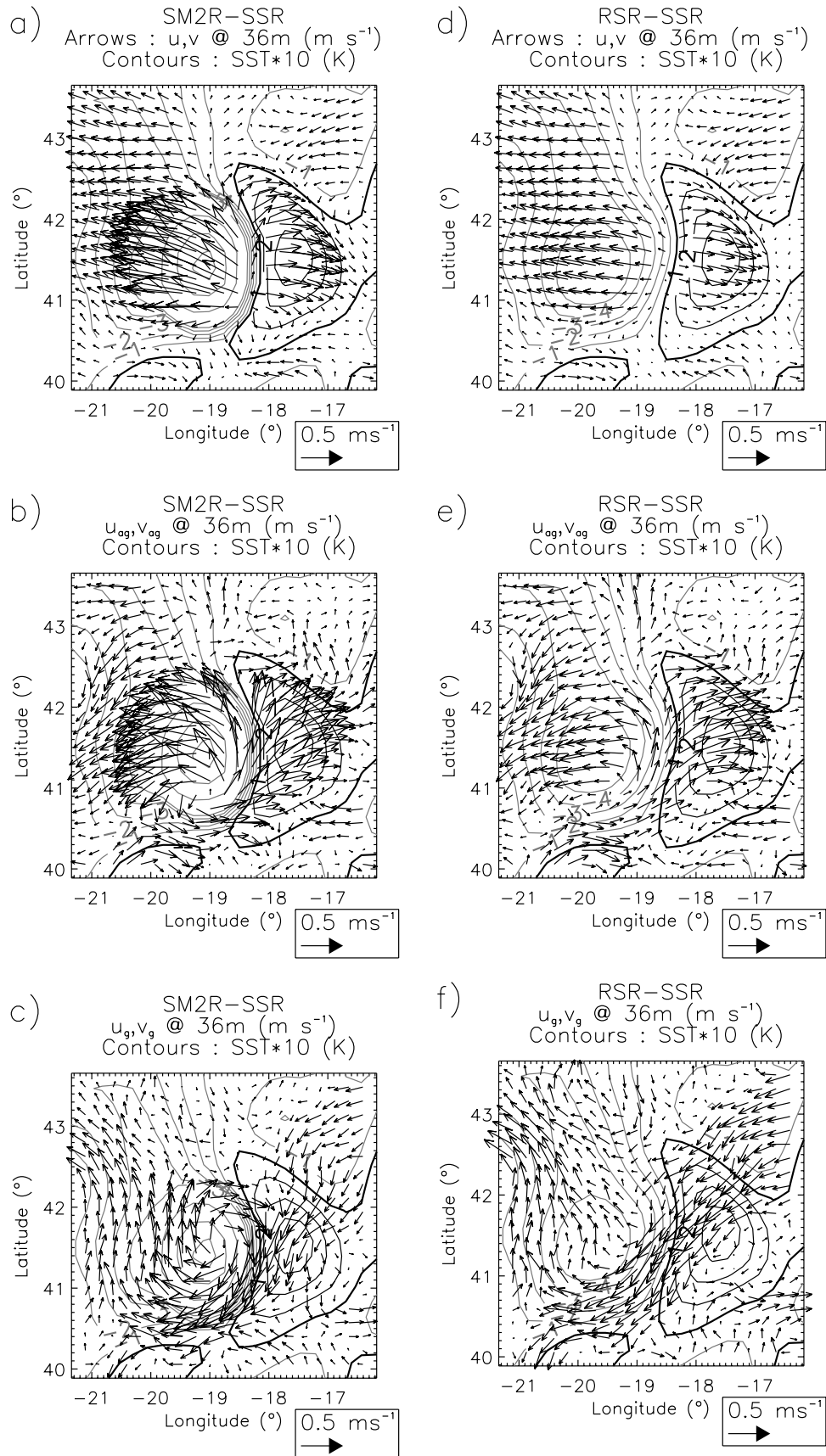
Figure 6

flow anomalies at surface level (compare Figures 6b and 6e to Figures 6a and 6d, respectively).

4.4. Thermal and Dynamical Structures in the Vertical Plane

[48] The anomalous (RSR minus SSR) vertical dynamical structure of the MABL consists of two distinct rolls with a common descending branch over the maximum surface thermal gradient zone, as shown in Figure 7b. The vertical cross section presented in Figure 7b is from 21.2W to 16.2W at 41.5N, which approximately lies in the wind direction. The rolls exhibited in Figure 7b are SCs since they do not appear in the reference run (Figure 7e). However, let us insist on the fact that the SCs in Figure 7b are anomalous SCs (ASCs hereafter). We chose to work on anomalies with respect to SSR, because the vertical dynamical structures of the MABL simulated in SM2R, RSR, and SSR did not differ greatly from each other (i.e., Figure 7e, which represents the SSR, is also representative of the RSR and SM2R). Thus the ASCs are not absolute (real) SCs.

[49] The vertical extent of the ASCs is similar in the RSR-SSR and the SM2R-SSR, i.e., ~1200 m (Figures 7a and 7b). The main difference between the RSR-SSR and the SM2R-SSR is that the western circulation (over the cold eddy) is reinforced in the SM2R-SSR. The existence of ASCs confirm the ageostrophic nature of the anomalous wind variations shown in section 4.3. Moreover, the associated surface convergence (1000 m divergence) shows that the wind slows down (accelerates) over the cold SST and accelerates (slows down) over the warm SST at surface level (1000 m). Figure 7 also reveals a modification in BLH, which is more important and localized (right at the vertical of the center of the cold eddy) in the SM2R. The maximum decrease (increase) in BLH over the cold (warm) water, for the RSR and SM2R are −48 m (+11 m) and −124 m (+10 m), respectively. Surprisingly, the vertical circulations reach the top of the boundary layer, despite the small SST gradients in the RSR.

[50] Although Figure 7 gives an idea of the shape of the ASCs, it does not exactly reflect the actual anomalous circulations, which are twisted by the Coriolis effect. Indeed, the average direction of the wind anomalies over the cold and warm eddies gradually turns by more than 180° clockwise with height, from the surface to the top of the MABL. Therefore the actual circulations look like vertical toroids, twisted clockwise from their top.

4.5. Analysis at 1000 m (MABL Top)

[51] Similarly to the surface level, the SM2R-SSR and RSR-SSR winds are mostly explained by their ageostrophic components at 980 m, as shown in Figures 8a and 8b and Figures 8d and 8e. The geostrophic components of the wind have two circulations, namely, a cyclonic circulation (i.e., a warm anomaly) over the cold

SST and an anticyclonic circulation (cold anomaly) over the warm SST (Figures 8c–8f). Note also that the associated temperature gradients at 980 m are one order of magnitude smaller than the surface level gradients (0.04°C per 100 km for the RSR-SSR and 0.05°C per 100 km for the SM2R-SSR). These results are remarkably consistent with the observations of *Hashizume et al.* [2002].

[52] *Hashizume et al.* [2002] hypothesized that the increase (decrease) in MABL mixing due to the warm (cold) SST raised (lowered) the MABL height, leaving a cold (warm) temperature anomaly near the top of the MABL. Figure 9 appears to confirm such an hypothesis for POMME. Indeed, the shapes of the anomalous profiles of temperature and pressure are very similar to the observed profiles in *Hashizume et al.* [2002]. In addition, the BLH is different on both sides of the SST front (last section). Finally, the sign of the temperature anomalies (temperature over the warm SST minus temperature over the cold SST) differs at 980 m and near the surface. The only difference is that the temperature and pressure profiles over the cold and warm SST do not reconnect before 2500 m, which is unexpectedly twice as high as the average BLH during POMME, and 700 m higher than in *Hashizume et al.* [2002].

5. Diagnosing Air Sea Interactions
5.1. GP2000 Equations

[53] Diagnostic equations are an efficient tool to directly determine the physical processes responsible for the generation of SCs. For our purpose, several equations could be used, such as the ω-equation of *Hoskins et al.* [1978] or the S−E equations. In the present manuscript, we used a 3-D general primitive form of the S−E equations, developed by GP2000. A unique feature of the GP2000 equations is that they express the production of ageostrophic circulations, as a function of their different sources, that is, friction, diabatic heating, and other geostrophic and ageostrophic sources. Thus the GP2000 equations are well suited for studies in the boundary layer. They are written as,

$$-f^2\frac{\partial u_{ag}}{\partial z}+\frac{\partial b}{\partial z}\frac{\partial w}{\partial x}=Q_{dmx}+Q_{thx}+Q_{dagx}+Q_{drx}+2Q_{twx}=Q_{totx} \quad (1)$$

$$-f^2\frac{\partial v_{ag}}{\partial z}+\frac{\partial b}{\partial z}\frac{\partial w}{\partial y}=Q_{dmy}+Q_{thy}+Q_{dagy}+Q_{dry}+2Q_{twy}=Q_{toty}, \quad (2)$$

where f is the Coriolis parameter, b is the buoyancy, w is the vertical wind component, u_{ag} and v_{ag} are the ageostrophic components of the wind, and the Q terms on the r.h.s are forcing terms, expressed in s^{-3}. They are

Figure 6. Simulated wind vector anomalies above the sea surface, and SST patterns. Positive (negative) SST anomalies are plotted in black (grey). The fields in Figures 6a, 6b, and 6c (Figures 6d, 6e, and 6f) correspond to the SM2R (RSR) minus the SSR, i.e., with respect to the reference run. (a, d) Horizontal wind vectors, (b, e) ageostropic components of the wind, and (c, f) geostrophic wind.
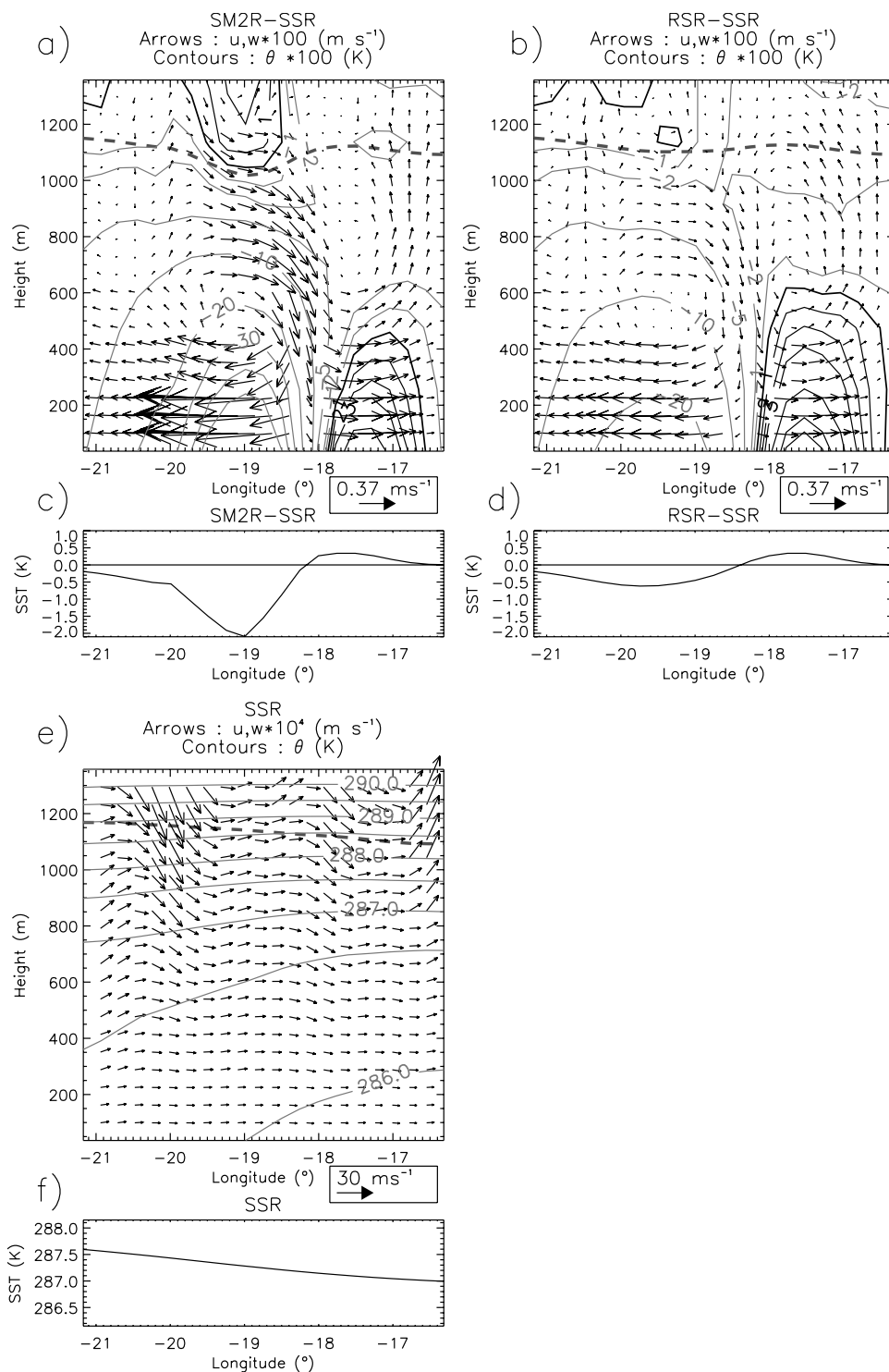
Figure 7. Thermal and dynamical vertical structure of the boundary layer along a cross section from 21.2W/41.5N to 16.2W/41.5N according to MM5 simulations. Figure 7a (Figure 7b) represents anomalies between runs SM2R (RSR) and SSR, while Figure 7e corresponds to SSR only. (a, b, e) Dashed lines locate the BLH. Positive (negative) temperature anomalies are plotted in black (grey). (c, d, f) SST variations along the cross section, in the SM2R-SSR, RSR-SSR, and SSR, respectively.

briefly described hereafter (see GP2000 for a full description). Before this and for a better understanding of the physical meaning of the Q terms, it should be recalled that the atmosphere always tends to restore the balance between the wind and the thermal configuration of the atmosphere. If for some reason there is a Thermal Wind Imbalance (TWI), then ageostrophic circulations are initiated in order to restore the balance. TWI may be
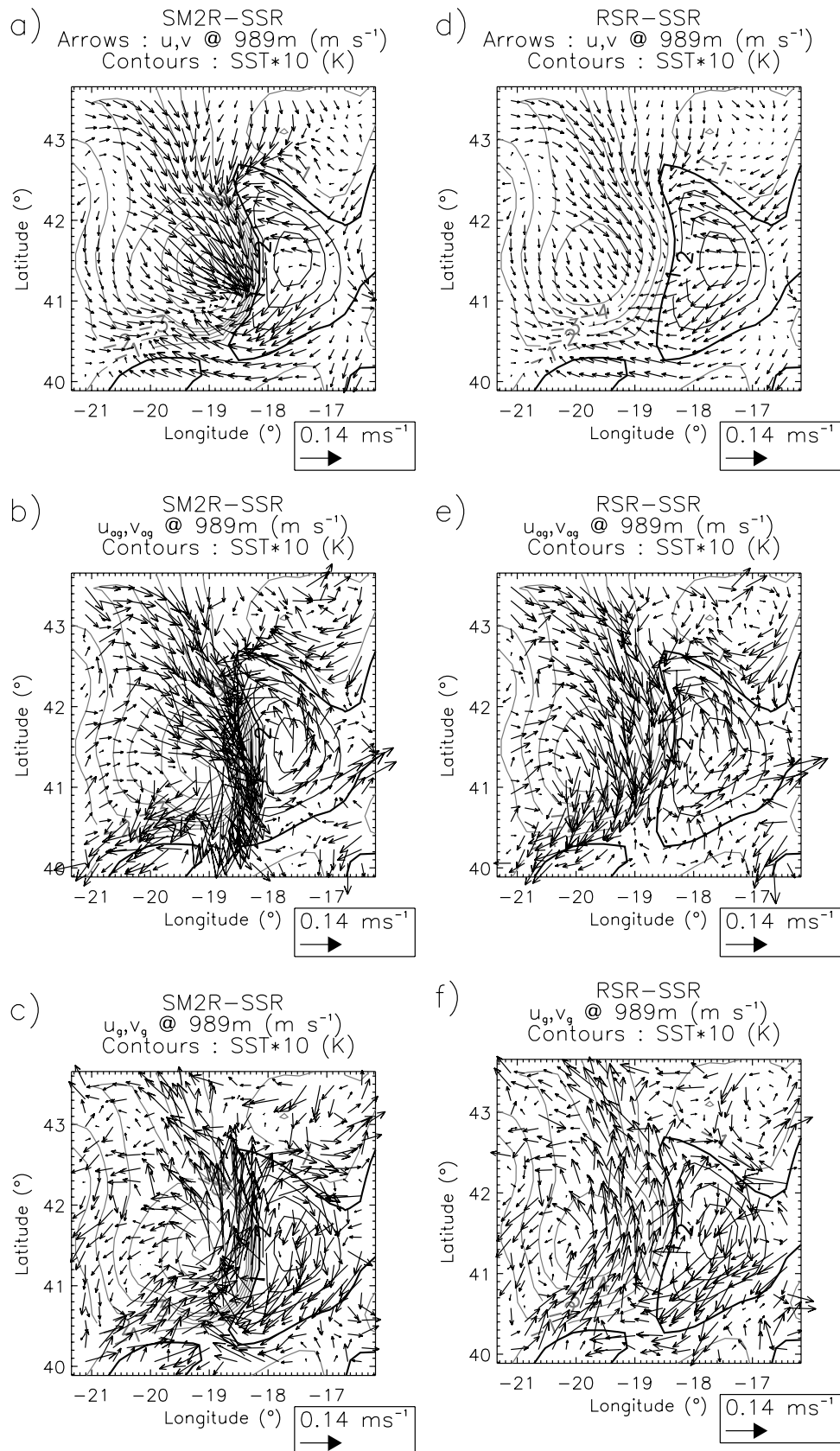
Figure 8. Simulated wind vector anomalies near the MABL top, and SST patterns. Positive (negative) SST anomalies are plotted in black (grey). The fields in Figures 8a, 8b, and 8c (Figures 8d, 8e, and 8f) correspond to the SM2R (RSR) minus the SSR, i.e., with respect to the reference run. (a, d) Horizontal wind vectors, (b, e) ageostropic components of the wind, and (c, f) geostrophic wind.
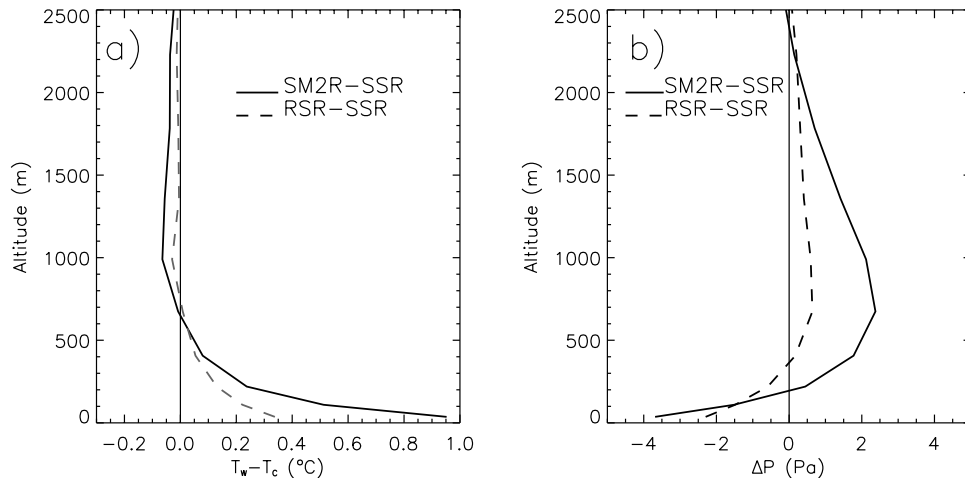
Figure 9. Differences in anomalous profiles (SM2R-SSR and RSR-SSR) of (a) temperature and (b) pressure between the warm and the cold side of the SST front.

caused by various sources, which are represented by the Q terms in equations (1) and (2).

[54] 1. Q_{th} is the turbulent heat forcing (thermal forcing term), i.e., the production of TWI that results from horizontal differential heating by turbulent heat fluxes.

[55] 2. Q_{dm} is the momentum flux forcing (dynamical forcing term), which is the effect of friction against surface, on the TWI.

[56] 3. Q_{tw} is the wind forcing (thermal forcing term). It represents the modification of the TWI through a perturbation of the thermal field by the geostrophic plus ageostrophic components of the wind.

[57] 4. Q_{dag} is the ageostrophic forcing (dynamical forcing term). It acts through differential advection of TWI (advection by the horizontal wind shear).

[58] 5. Q_{dr} is the residual ageostrophic forcing (dynamical forcing term), that is, the local trend of TWI.

[59] 6. Q_{tot} is the total forcing.

[60] In the following, the domain under consideration is restricted to the cross section where ASCs were shown in section 4.4, i.e., a vertical section from 21.2W to 16.2W at constant latitude (41.5N), the x axis being the across front axis, directed from the negative to the positive SST anomaly.

[61] The r.h.s. and l.h.s. terms of equation (1) were evaluated each day of the IOP, every three hours, for the SSR, RSR, and SM2R. Next, the different terms were averaged from February to April 2001. At surface level, the dominant term in the r.h.s. of equation (1) is clearly Q_{dmx}, i.e., friction, for both SM2R-SSR and RSR-SSR (Figures 10a and 10b). The peaks in Q_{dmx} are located over the extrema of SST. Forcings other than Q_{dmx} have a small impact on the total forcing Q_{totx}, except maybe Q_{dagx} and Q_{drx}. As a result, thermal forcings are negligible compared to dynamical forcings. In other words, the effects of friction dominate those of heat fluxes (and subsequently, baroclinicity), which will be further investigated in section 5.2.

[62] At the top of the MABL, the different forcings have a magnitude that is decreased by a factor 10 compared to surface, as shown in Figures 10c and 10d. In spite of that, Q_{dmx} is still well correlated to the variations of Q_{totx}. Q_{thx} also contributes to the production of ageostrophic circulations at 1000 m. However, its effect is largely compensated

by Q_{drx}. The contributions of Q_{thx} and Q_{drx} are clearly out of phase and have the largest amplitude at the location of the maximum SST gradients, that is, in the neighborhood of the ascending and descending branches of the ASCs. The fact that Q_{drx} and Q_{thx} cancel out without contributing to the r.h.s. of equation (1) means that part of the energy communicated to the flow through differential heating (Q_{thx}) directly opposes to this heating (Q_{drx}), whereas the remaining energy feeds a cross frontal circulation through Q_{dmx}. Such a process does not comply with a traditional view of the problem of geostrophic adjustment, in many respects. In particular, Q_{twx} is usually not negligible as its definition explains part of the feedback of the ageostrophic circulation on the thermal structure of the MABL (see GP2000). Although the kind of adjustment found in the present case cannot be rejected off-hand, a possible source of error is the very short spin-up time (3 to 24 hours) when the model was run, which could affect the balance between the different forcing terms.

5.2. Relationship Between the Friction Term and Boundary Layer Stability

[63] In the context of POMME, the leading process that drives the response of the lower part of the MABL to a SST contrast is friction at the sea surface, as shown in the last section. This is further investigated hereafter.

[64] The leading physical process responsible for the variations of friction is stability, because of its effect on the roughness length or on the drag coefficient, as already hypothesized by *Hayes et al.* [1989] and others. In this section, one investigates the validity of this hypothesis for POMME. More precisely, one investigates the effect of stability on the friction term in equation (1), that is, Q_{dmx}, which is defined as,

$$Q_{dmx} = -f \frac{\partial}{\partial z} \left(\frac{1}{\rho} \frac{\partial \tau_{y\alpha_i}}{\partial \alpha_i} \right), \qquad (3)$$

where τ is the turbulent momentum flux and α_i is now reduced to z for simplicity. As equation (3) is not a standard output of MM5, it was necessary to recalculate it. The MRF model was applied "off line" to the wind,
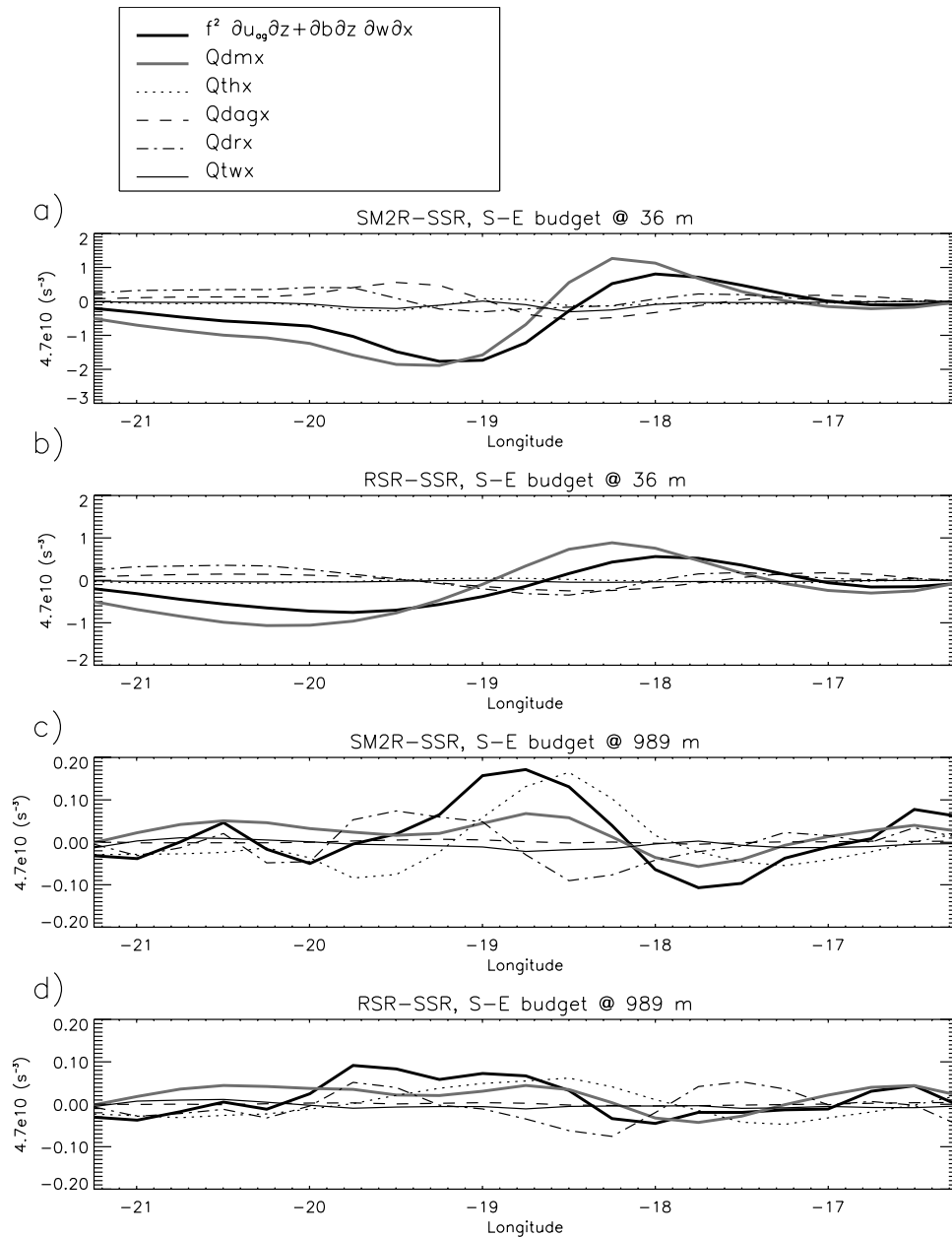
Figure 10. Budget of the GP2000 equation for the across front component of the ageostrophic wind. The fields in Figures 10a and 10c (Figures 10b and 10d) correspond to the SM2R (RSR) minus the SSR.

temperature, pressure and humidity values simulated during the SSR, RSR, and SM2R. Because the calculation of vertical derivatives is not accurate with only a few levels in the boundary layer, an additional independent calculation of Q_{dmx} was performed. First, the divergence of the momentum flux was derived as the residual of the momentum conservation equation. Next, the expression was derived with respect to the vertical axis. The calculated and residual Q_{dmx} are in good agreement, as shown in Figures 11a and 11c, and Figures 11b and 11d. In order to show the effect of stability on Q_{dmx}, the latter expression was recalculated with a constant, neutral stability.

[65] The comparison between the expressions recalculated with and without stability is presented in Figures 11c and 11e and Figures 11d and 11f. It clearly shows that the

spatial anomalies of the vertical derivative of the momentum flux would have had an opposed sign if the MABL had been neutral. This shows that the effect of SST on friction is mainly due to stability. However, it is possible to claim that the calculation in the neutral case is not meaningful since the wind and temperature profiles used for the calculation have already been affected by stability. This is one limitation of the approach.

6. Conclusions

[66] A quasi steady oceanic eddy associated with SSTs colder than their environment was found during the IOP of the POMME experiment, in the northeast Atlantic. The radius of the eddy was 90 km, and the SST anomaly was $\sim 1°C$ per 100 km.
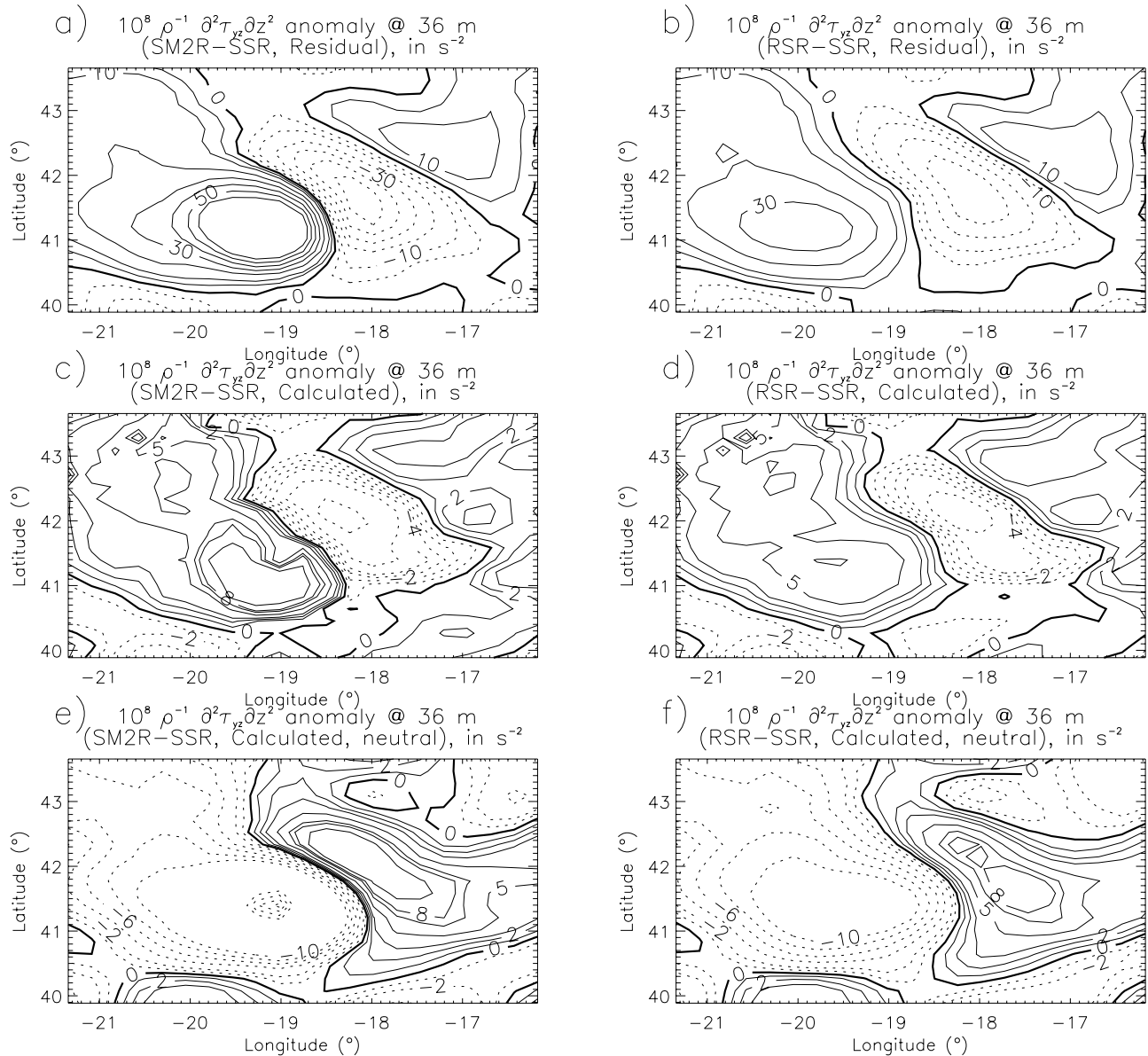
Figure 11. Secondary derivative along the vertical of the vertical momentum flux along the y axis, at surface level. (a, b) Flux is the residual of the momentum conservation equation, and (c, d) it was recalculated. (e, f) Stability was assumed to be neutral in the calculation of the flux. Positive (negative) contours are plotted in full (dotted) line.

[67] Interpolated buoy data and satellite-derived observations revealed that signatures of the cold eddy were present in surface wind and net heat flux fields, for 3-month averages. The relationship between SST and wind anomalies also appeared, though less clearly, in an analysis of daily data.

[68] A meteorological model was used to simulate the MABL during the IOP, with different SST fields in which the cold eddy was present or not, as surface boundary conditions. The simulations showed that mesoscale wind and net heat flux anomalies consistent with satellite observations developed over the cold eddy, when the cold eddy was present in the forcing fields. As a result, the cold eddy affected the wind and net flux patterns. Additionally, if the amplitude of the SST gradient was exaggerated ($\sim$2°C per 100 km) in the forcing fields, then it significantly affected not only the wind and surface net heat flux, but also the downward radiative fluxes and the integrated liquid water content in the atmosphere. The effect of the cold eddy was to decrease (increase) the longwave (shortwave) flux and to decrease the integrated liquid water content.

[69] The simulations did not show the presence of secondary circulations. However, they clearly revealed the existence of anomalous secondary circulation, with respect to a reference run. The latter circulations presented a divergence zone located downstream the cold eddy, consistent with *Businger and Shaw*'s [1984] heat island effect. We found that the anomalous circulations extended over the whole boundary layer ($\sim$1200 m). This result may seem surprising at first glance, because in previous studies the

effect of a weak SST gradient was only to generate an IBL [GP2000, *Rogers*, 1989]. One possible explanation is the fact that the timescales involved are different: our results are averages over three months, whereas GP2000 considered an individual case.

[70] The MABL responded differently near the surface and in the vicinity of the BLH. At surface level (near the boundary layer top), the wind decreased (increased) over the cold SST, as a result of the interaction between the circulations and the synoptic wind. Above 600 m, the sign of the horizontal temperature gradient was found to be opposed to the sign of the underlying SST gradient. This is consistent with the results of *Hashizume et al.* [2002], who explain this phenomenon by the displacement of the BLH under the effect of eddy mixing variations.

[71] Both near the surface and above 600 m, the anomalous wind patterns were mostly explained by their ageostrophic component. In order to analyze the origin of the anomalous ageostrophic wind, diagnostic equations were used. It was shown that friction was generally the leading term that explained the production of cross frontal ageostrophic wind at surface. Near the top of the boundary layer, the effect of horizontal gradients of heat fluxes (thus buoyancy), also contributed to the generation of ageostrophic wind. The latter forcing term was out of phase with the local trend of along front thermal wind imbalance. This suggests that most of the energy injected in the flow through differential heating is directly balanced by the local trend of thermal wind imbalance and does not contribute to the generation of cross frontal circulations, at the top of the MABL. At surface level, variations of dynamical stability were found to be responsible for the spatial variations of the momentum flux forcing term in the diagnostic equations.

[72] The results presented in this paper showed that a weak SST anomaly could significantly affect the MABL, depending on the timescale considered. One of the most obvious effects of the SST anomaly was a modification of the mesoscale patterns of surface winds. This raises the issue of the global impact of weak SST anomalies on atmospheric variability, a topic that was recently well documented by *Xie* [2004]. Such SST anomalies are present over most of the world's ocean, and could therefore have a significant impact on climate variability.

References

Assenbaum, M., and G. Reverdin (2004), Near real-time analyses of the mesoscale circulation during the POMME experiment, *Deep Sea Res.*, in press.
Betts, A. K., S.-H. Hong, and H.-L. Pan (1996), Comparison of NCEP-NCAR reanalysis with 1987 FIFE data, *Mon. Weather Rev.*, 124, 1480–1498.
Bourras, D., L. Eymard, and W. T. Liu (2002a), A neural network to estimate the latent heat flux over oceans from satellite observations, *Int. J. Remote Sens.*, 23, 2405–2423.
Bourras, D., L. Eymard, W. T. Liu, and H. Dupuis (2002b), An integrated approach to estimate instantaneous near-surface air temperature and sensible heat flux fields during the SEMAPHORE experiment, *J. Appl. Meteorol.*, 41, 241–252.
Bourras, D., W. T. Liu, L. Eymard, and W. Tang (2003), Evaluation of latent heat flux fields from satellites and models during the SEMAPHORE experiment, *J. Appl. Meteorol.*, 42, 227–239.
Brisson, A., P. LeBorgne, A. Marsouin, and T. Moreau (1994), Surface irradiances calculated from Meteosat sensor data during SOFIA-ASTEX, *Int. J. Remote Sens.*, 15, 197–203.
Businger, J. A., and W. J. Shaw (1984), The response of the marine boundary layer to mesoscale variations in sea-surface temperature, *Dyn. Atmos. Oceans*, 8, 267–281.
Carlson, T. N., and F. E. Boland (1978), Analysis of urban-rural canopy using a surface heat flux/temperature model, *J. Appl. Meteorol.*, 17, 998–1013.
Chelton, D. B., S. K. Esbensen, M. G. Schlax, N. Thum, F. Wentz, C. L. Gentemann, M. J. McPhaden, and P. S. Schopf (2001), Observation of coupling between surface wind stress and sea surface temperature in the eastern tropical Pacific, *J. Clim.*, 14, 1479–1498.
Cronin, M. F., S.-P. Xie, and H. Hashizume (2003), Barometric pressure variations associated with eastern Pacific tropical instability waves, *J. Clim.*, 16, 3050–3057.
Ducet, N., P. Y. Le Traon, and G. Reverdin (2000), Global high-resolution mapping of ocean circulation from TOPEX/Poseidon and Ers-1 and -2, *J. Geophys. Res.*, 105, 19,477–19,498.
Dudhia, J. (1993), A nonhydrostatic version of the Penn State-NCAR Mesoscale Model: Validation tests and simulation of an Atlantic cyclone and cold front, *Mon. Weather Rev.*, 121, 1493–1513.
Eliassen, A. (1962), On the vertical circulation in frontal zones, *Geophys. Norv.*, 24, 147–160.
Eymard, L., et al. (1996), Study of the air-sea interactions at the mesoscale: The SEMAPHORE experiment, *Ann. Geophys.*, 14, 986–1015.
Friehe, C. A., W. J. Shaw, D. P. Rogers, K. L. Davidson, W. G. Large, S. A. Stage, G. H. Crescenti, S. J. S. Khalsa, G. K. Greenhut, and F. Li (1991), Air-sea fluxes and surface layer turbulence around a sea surface temperature front, *J. Geophys. Res.*, 96, 8593–8609.
Gérard, E., and L. Eymard (1998), Remote sensing of integrated cloud liquid water: Development of algorithms and quality control, *Radio Sci.*, 33, 433–447.
Giordani, H., and S. Planton (2000), Modeling and analysis of ageostrophic circulation over the Azores oceanic front during the SEMAPHORE experiment, *Mon. Weather Rev.*, 128, 2270–2287.
Giordani, H., S. Planton, B. Bénech, and B.-H. Kwon (1998), Atmospheric boundary layer response to sea surface temperatures during SEMAPHORE experiment, *J. Geophys. Res.*, 103, 25,047–25,060.
Goodberlet, M. A., C. T. Swift, and J. C. Wilkerson (1990), Ocean surface wind speed from the Special Sensor Microwave/Imager (SSM/I), *IEEE Trans. Geosci. Remote Sens.*, 28, 823–828.
Hashizume, H., S.-P. Xie, M. Fujiwara, M. Shiotani, T. Watanabe, Y. Tanimoto, W. T. Liu, and K. Takenchi (2002), Direct observations of atmospheric boundary layer response to SST variations associated with tropical instability waves over the eastern equatorial Pacific, *J. Clim.*, 15, 3379–3393.
Hayes, S. P., M. J. McPhaden, and J. M. Wallace (1989), The influence of sea-surface temperature on surface wind in the eastern equatorial Pacific: Weekly to monthly variability, *J. Clim.*, 2, 1500–1506.
Hong, S.-Y., and H.-L. Pan (1996), Nonlocal boundary layer vertical diffusion in a medium-range forecast model, *Mon. Weather Rev.*, 124, 2322–2339.
Hoskins, B. J., I. Draghici, and H. C. Davies (1978), A new look at the ω-equation, *Q. J. R. Meteorol. Soc.*, 104, 31–38.
Khalsa, S. J. S., and G. K. Greenhut (1989), Atmospheric turbulence structure in the vicinity of an oceanic front, *J. Atmos. Sci.*, 42, 1283–1305.
Kwon, B.-H., B. Bénech, D. Lambert, P. Durand, A. Druilhet, H. Giordani, and S. Planton (1998), Structure of the marine atmospheric boundary layer over an oceanic thermal front: SEMAPHORE experiment, *J. Geophys. Res.*, 103, 25,159–25,180.
Pollard, R. T. (1978), The Joint Air-Sea Interaction Experiment—JASIN 1978, *Bull. Am. Meteorol. Soc.*, 59, 1310–1318.
Rogers, D. P. (1989), The marine boundary layer in the vicinity of an ocean front, *J. Atmos. Sci.*, 46, 2044–2062.
Sawyer, J. S. (1956), The vertical circulation at meteorological fronts and its relation to frontogenesis, *Proc. R. Soc. London, Ser. A.*, 234, 346–362.
Stage, S. A., and R. A. Weller (1985), The Frontal Air-Sea Interaction Experiment (FASINEX); part I: Background and scientific objectives, *Bull. Am. Meteorol. Soc.*, 66, 1511–1520.
Sweet, W., R. Fett, J. Kerling, and P. LaViolette (1981), Air-sea interaction effects in the lower troposphere across the north wall of the Gulf Stream, *Mon. Weather Rev.*, 109, 1042–1052.

Wallace, J. M., T. P. Mitchell, and C. Deser (1989), The influence of sea-surface temperature on surface wind in the eastern equatorial Pacific: Seasonal and interanual variability, *J. Clim.*, *2*, 1492–1499.

Warner, T. T., M. N. Lakhtakia, J. D. Doyle, and R. A. Pearson (1990), Marine atmospheric boundary layer circulations forced by Gulf Stream sea surface temperature gradients, *Mon. Weather Rev.*, *118*, 309–323.

Wexler, R. (1946), Theory and observation of land and sea breezes, *Bull. Am. Meteor. Soc.*, *27*, 272–287.

White, W. B., and J. L. Annis (2003), Coupling of extratropical mesoscale eddies in the ocean to westerly winds in the atmospheric boundary layer, *J. Phys. Oceanogr.*, *33*, 1095–1107.

Woodruff, S. D., R. J. Slutz, R. L. Jenne, and P. M. Steurer (1987), A comprehensive ocean-atmosphere data set, *Bull. Am. Meteorol. Soc.*, *68*, 1239–1250.

Xie, S.-P. (2004), Satellite observations of cool ocean-atmosphere interaction, *Bull. Am. Meteorol. Soc.*, *2*, 195–207.

Xie, S.-P., M. Ishiwatari, H. Hashizume, and K. Takeuchi (1998), Coupled ocean-atmospheric waves on the equatorial front, *Geophys. Res. Lett.*, *25*, 3863–3866.

—————————

D. Bourras, IPSL-CETP-CNRS, UMR 8639, 10-12 Avenue de l'Europe, 78140 Vélizy-Villacoublay, France. (denis.bourras@cetp.ipsl.fr)

G. Caniaux and H. Giordani, Centre National de Recherches Météorologiques, 31057 Toulouse, France.

G. Reverdin, Laboratoire d'Océanographie Dynamique et de Climatologie, 75252 Paris, France.